RESEARCH ARTICLE

A densification mechanism to model the mechanical effect of methane hydrates in sandy sediments

Maria De La Fuente[1,2] ⓘ | Jean Vaunat[3] ⓘ | Héctor Marín-Moreno[1] ⓘ

[1]National Oceanography Centre, University of Southampton Waterfront Campus, European Way, Southampton, UK

[2]Ocean and Earth Science, University of Southampton, European Way, Southampton, UK

[3]Department of Civil and Environmental Engineering, Universitat Politècnica de Catalunya, Barcelona, Spain

Correspondence
M. De La Fuente, National Oceanography Centre, University of Southampton Waterfront Campus, European Way, Southampton SO14 3ZH, UK.
Email: mdlf1g15@soton.ac.uk

SUMMARY

Recent pore-scale observations and geomechanical investigations suggest the lack of true cohesion in methane hydrate-bearing sediments (MHBSs) and propose that their mechanical behavior is governed by kinematic constrictions at pore-scale. This paper presents a constitutive model for MHBS, which does not rely on physical bonding between hydrate crystals and sediment grains but on the densification effect that pore invasion with hydrate has on the sediment mechanical properties. The Hydrate-CASM extends the critical state model Clay and Sand Model (CASM) by implementing the subloading surface model and introducing the densification mechanism. The model suggests that the decrease of the sediment available void volume during hydrate formation stiffens its structure and has a similar mechanical effect as the increase of sediment density. In particular, the model attributes stress-strain changes observed in MHBS to the variations in sediment available void volume with hydrate saturation and its consequent effect on isotropic yield stress and swelling line slope. The model performance is examined against published experimental data from drained triaxial tests performed at different confining stress and with distinct hydrate saturation and morphology. Overall, the simulations capture the influence of hydrate saturation in both the magnitude and trend of the stiffness, shear strength, and volumetric response of synthetic MHBS. The results are validated against those obtained from previous mechanical models for MHBS that examine the same experimental data. The Hydrate-CASM performs similarly to previous models, but its formulation only requires one hydrate-related empirical parameter to express changes in the sediment elastic stiffness with hydrate saturation.

KEYWORDS

densification mechanism, constitutive modeling, Hydrate-CASM, mechanical behavior, methane hydrate-bearing sediments

1 | INTRODUCTION

Methane hydrates have drawn international interest as an alternative energy resource to conventional fossil fuels,[1-5] and as a major hazard for offshore drilling and gas production operations,[6-8] global climate change,[9-12] and seafloor instability.[13-15] Quantitative evaluation of the resource potential of gas hydrate reservoirs and of their response to

natural and/or human-induced changes in pressure and temperature (P-T) conditions requires precise knowledge of the hydrate phase change phenomenon and of its effect on the mechanical stability of the reservoir. Due to the operational complexity at preserving the in situ P-T conditions during methane hydrate-bearing sediment (MHBS) recovery, the mechanical properties of these sediments are generally investigated through geophysical techniques[16-18] and geotechnical testing of synthetic sediments.[19-21] Both geophysical and geotechnical data show that the stiffness, strength, and dilatancy of MHBS tend to increase with increasing hydrate saturation.[22,23] They also evidence that their mechanical and hydraulic properties drastically change during hydrate dissociation, which may compromise the mechanical stability of the sediment. Thus, hydrate dissociation is likely to trigger small to large-scale deformations in the seabed, including sediment collapse[24] and sliding.[25-27] As a result, dissociation may also induce damage of preexisting offshore infrastructures.[28]

Several mechanical models developed for MHBS assume that the increase of strength, stiffness, and dilatancy observed in these sediments is mainly governed by bonding or cementation between the hydrate crystal and the sediment grains (Table 1). However, recent pore-scale observations[40-42] and geomechanical investigations[43-45] evidence the lack of true cohesion in MHBS and suggest that the mechanical response of these sediments may not necessarily be governed by sediment bonding/cementation, but rather to kinematic constrictions at pore/grain scale during shearing. In this paper, we develop a new mechanical constitutive model that does not consider hydrate-bonding effects in its formulation but assumes that the reduction of sediment available void volume and the increase of sediment elastic stiffness during pore invasion with hydrate can explain the greater mechanical properties observed in MHBS.

The elasto-plastic model Hydrate-CASM extends the formulation of the unified critical state constitutive model CASM[46] by implementing the subloading surface model[47] and introducing the densification mechanism. The subloading surface, which has been successfully used in previous mechanical models for MHBS,[33,34,38,48] allows capturing irrecoverable plastic strains inside the yield surface. The densification mechanism suggests that the decrease of the available void volume of the host sediment during hydrate formation stiffens its structure and has a similar mechanical effect as the increase of the sediment density. In particular, the densification mechanism attributes the stress-strain changes observed in MHBS to variations in sediment available void volume with hydrate saturation and its consequent effect on isotropic yield stress and swelling line slope.

The Hydrate-CASM is applied here to robust and well-described published experimental data[19,21] that cover the most relevant conditions related to MHBS behavior, including a wide range of hydrate saturations, several hydrate morphologies, and confinement stress. These data have also been used in the calibration of previous mechanical models developed for MHBS,[33,34,48,74,79] which give us the opportunity to compare and validate our results. The model performance is found satisfactory over a wide range of test conditions and evidence the capability of the Hydrate-CASM model at capturing both the trend and magnitude of the stress-strain and the volumetric response of synthetic MHBS. In addition, the good matching of our results with the outputs obtained from previous mechanical models for MHBS evidences that the experimental data examined in this paper can be simply reproduced by (a) considering the mechanical effect of the reduction of sediment available void volume due to pore invasion with hydrate and (b) modifying the sediment elastic stiffness according to hydrate saturation. Our results also show that accounting for the different initial void ratios of the set of host specimens used to produce

TABLE 1 Notable mechanical models for MHBS considering hydrate-bonding effect

Model Reference	Hydrate-Bonding Modeling Strategy
Klar et al[29]; Jung et al[30]; Pinkert and Grozic[31]; Pinkert et al[32]	Additional cohesion constituent in the failure criteria
Uchida et al[33]; Sánchez and Gai[34]; Sánchez et al[35]	Enlargement of the yield surface by cohesion and dilatation
Sultan and Garziglia[36]	Impediment of the normal consolidation of the sediment and enlargement of the yield surface
Sánchez and Gai[34]; Sánchez et al[35]; De La Fuente et al[37]	Stress-strain partition between hydrate and matrix in a bonding damage framework
Jiang et al[38]	Attribution of physical bonding properties in discrete element methods
Lin et al[39]	Expansion of the failure envelope in a spatially mobilized plane model

Abbreviation: MHBS: methane hydrate-bearing sediment.

cementing and pore-filling MHBS allows capturing the experimental data without using any empirical parameters related to the hydrate morphology.

2 | CASM MODEL

The Hydrate-CASM extends the formulation of the constitutive model CASM developed by Yu.[46] The CASM model is selected here because of its simplicity and flexibility in describing the shape of the yield surface as well as its proven ability to predict the mechanical behavior of sand, the most likely target for the commercial exploitation of hydrates.[49] The critical state model CASM is formulated in terms of the state parameter[50] and the spacing ratio concept and uses a non-associated flow rule, which is particularly suitable to simulate the behavior of granular sediments like those examined in this paper.[51,52] All the parameters used in the formulation are listed and defined in Table 2.

2.1 | State parameter concept

The state parameter (Equation 1) is defined in the $v - \ln(p')$ space as the vertical distance between the void ratio at the current state and that at the critical state for a given mean effective stress (Figure 1A):

$$\xi = v + \lambda \ln(p') - \Gamma. \tag{1}$$

The magnitude and sign of this parameter play a key role in understanding the densification mechanism introduced in this paper. The state parameter adopts positive values when the sediment void ratio is located above the critical state line (CSL) (as in loose sand; Figure 1A), and negative ones when located below it (as in dense sand; Figure 1C). Sediments with a positive value of ξ and subjected to triaxial shear tend to show hardening on the $p' - q$ stress space and contractancy as volumetric response (Figure 1B). Instead, sediments with a negative value of ξ show a distinctive peak in the deviatoric stress followed by softening before the critical state is achieved, and dilatancy dominates its volumetric response (Figure 1D).

2.2 | CASM yield function

A total of seven model parameters are required to define the original CASM formulation. Five of which (λ, M, Γ, κ and v), are the same as those in the Cam Clay model,[53,54] and the two additional parameters, denoted by n and r, are used to specify the geometrical properties of the yield function. For a general stress state, the CASM yield function is expressed as:

$$f = \left(\frac{q}{Mp'}\right)^n + \frac{1}{\ln(r)} ln\left(\frac{p'}{p'_0}\right) \tag{2}$$

where n governs the shape of the yield surface and r controls its intersection with the CSL. Particular combinations of n and r allow the intersection between the CSL and the yield surface to not necessarily occur at the maximum deviatoric stress (Figure 2) as happens in Cam-Clay type models. This allows the CASM model to predict local peaks in the deviatoric stress on the left side of the critical state condition, feature that is widely observed in geotechnical testing of sand.[55,56] Certain values of n and r can also recover the yield surface function of the standard and modified Cam-clay models.[46]

Within the yield surface, the behavior is assumed isotropic and elastic, with the elastic volumetric stress-strain relationship governed by the bulk modulus K (Equation 3a) and the elastic shear by the shear modulus G (Equation 3b):

$$K = \frac{(1+e)p'}{\kappa} \tag{3a}$$

TABLE 2 CASM and Hydrate-CASM parameters

Model Parameters		Description
Stress	P_p	Pore pressure
	$\boldsymbol{\sigma}$	Cauchy total stress tensor
	$\mathbf{I}$	Identity matrix
	$\boldsymbol{\sigma}'$	Cauchy effective stress tensor, $\boldsymbol{\sigma}' = \boldsymbol{\sigma} - P_p\mathbf{I}$
	$\boldsymbol{\sigma_c}$	Confining total stress
	$\boldsymbol{\sigma}'_{\boldsymbol{c}}$	Confining effective stress, $\boldsymbol{\sigma}'_{\boldsymbol{c}} = \boldsymbol{\sigma_c} - P_p\boldsymbol{I}$
	p	Mean stress, $p = \frac{1}{3}(\sigma_1 + \sigma_2 + \sigma_3)$
	q	Deviatoric stress, $q = \sigma_1 - \sigma_3$
	p'	Mean effective stress, $p' = p - P_p$
	η	Stress ratio $\eta = q/p'$
Strain	$\boldsymbol{\varepsilon}$	Total infinitesimal strain tensor
	$\boldsymbol{\varepsilon}^e$	Elastic strain tensor
	$\|d\varepsilon^p\|$	Norm of the incremental plastic strain vector
	ε_v^p	Plastic volumetric strain, $\varepsilon_v^p = \varepsilon_1^p + \varepsilon_2^p + \varepsilon_3^p$
	ε_q^p	Plastic deviatoric strain, $\varepsilon_q^p = \frac{2}{3}(\varepsilon_1^p - \varepsilon_3^p)$
Volumetric ratios	V_t	Total volume
	V_s	Volume of mineral grains
	V_h	Volume of hydrate
	V_v	Potential void volume, $V_v = V_t - V_s$
	V_a	Available void volume, $V_a = V_v - V_h$
	e	Void ratio of the host sediment, $e = V_v/V_s$
	S_h	Hydrate saturation, $S_h = V_h/V_v$
	e_h	Hydrate ratio, $e_h = V_h/V_s = S_h e$
	e_{a_h}	Available void ratio of the hydrate-bearing sediment, $e_{a_h} = e(1 - S_h)$
	v	Specific volume, $v = 1+e$
	v_h	Hydrate-CASM equivalent specific volume, $v_h = v - e_h$
Critical state parameters	λ	Slope of the normal compression and critical state lines in the $v - ln(p')$ space
	M	Critical state stress ratio: slope of critical state line in the $p' - q$ space
	p_0	Isotropic yield stress of the host sediment
	p_{0_h}	Isotropic yield stress of the hydrate-bearing sediment
	p'_x	Mean effective stress at critical state
	Γ	Specific volume at critical state with p' of 1 KPa
Elastic parameters	κ	Host sediment swelling (reloading-unloading) line slope
	κ_h	MHBS swelling (reloading-unloading) line slope
	ν	Poisson's ratio
	K	Elastic bulk modulus
	G	Elastic shear modulus
	$\boldsymbol{D}^e$	Elastic stiffness tensor
CASM parameters	n	Stress-state coefficient: yield surface shape parameter
	r	Spacing ratio, $r = p'_0/p'_x$
	ξ	State parameter
	ξ_r	Reference state parameter, $\xi_r = (\lambda - \kappa)\ln r$

TABLE 2 (Continued)

Model Parameters		Description
Subloading parameters	p_{0_s}	Isotropic yield stress of the subloading surface
	R	Subloading surface ratio, $R = p_{0_s}/p_0$
	u	Subloading parameter controlling plastic deformations before yielding
Plastic parameters	φ	Size parameter
	χ	Vector of hardening (2 components: p_{0_h} and R)
	H	Hardening modulus
	λ^P	Plastic multiplier
Empirical parameters	κ_{rf}	Swelling line reduction factor

Note. Subscript h refers to hydrate-bearing sediment properties, and bold symbols denote tensors. Note that e_{ah}, v_h, p_{0_h} and κ_h recover the hydrate-free parameters e, v, p_0 and κ when $S_h = 0$.

Abbreviations: CASM: Clay and Sand Model; MHBS: methane hydrate-bearing sediment.
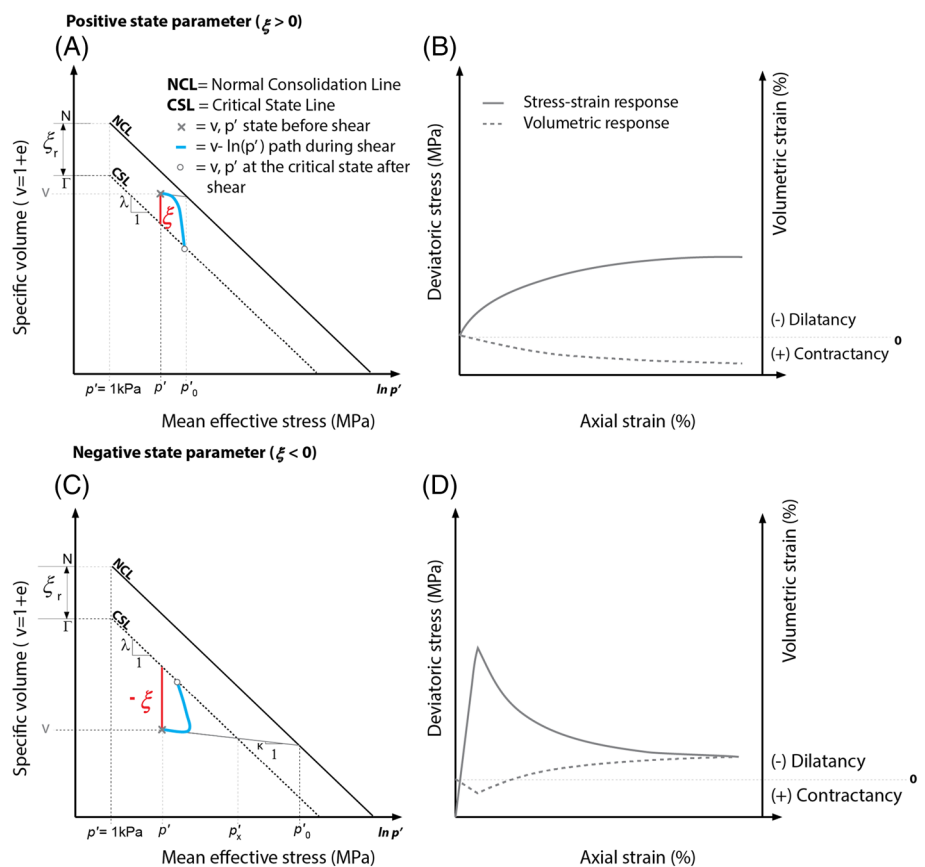
FIGURE 1 Clay and Sand Model (CASM) framework. Graphical representation of the CASM parameters and qualitative mechanical response of sediments subjected to triaxial shear with (A, B) positive and (C, D) negative values of ξ. After Yu[46]

$$G = \frac{3K(1-2\nu)}{2(1+\nu)} \tag{3b}$$

2.3 | Stress-dilatancy relation and plastic potential

The CASM model uses a non-associated flow rule that follows the stress-dilatancy law proposed by Rowe,[57] which has been applied with success at describing the deformation of sands and granular materials,[46] as well as to simulate the response of MHBS[43,44]:
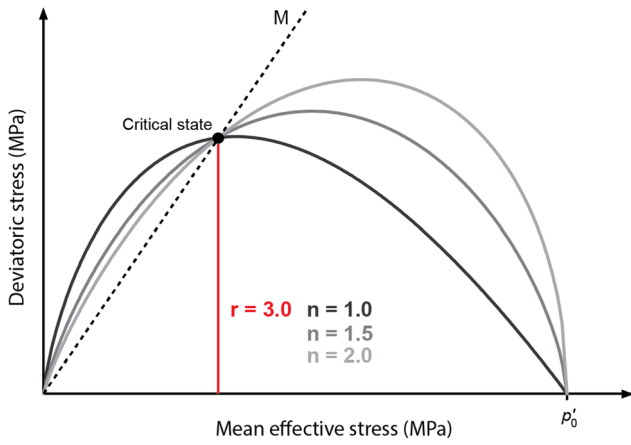
FIGURE 2 Influence of n and r in the shape and size of the yield surface. Note the presence of local peaks in the deviatoric stress on the left side of the critical state condition. After Yu[46]

$$\frac{d\varepsilon_v^p}{d\varepsilon_q^p} = \frac{9(M-\eta)}{9+3M-2M\eta} \tag{4}$$

By integrating Equation 4, the CASM plastic potential function is obtained as:

$$g = 3M\ln\left(\frac{p'}{\varphi}\right) + (3+2M)\ln\left(\frac{2q}{p'}+3\right) + (M-3)\ln\left(3-\frac{q}{p'}\right) \tag{5}$$

Whose expression does not depend on the hardening parameters and where φ is a size parameter controlling the size of the plastic potential which passes through the current stress state $(p'-q)$.

2.4 | Hardening parameters

Similar to Cam-clay type models, the CASM model assumes isotropic changes in the isotropic yield stress controlled by the incremental plastic volumetric deformation, so that:

$$dp_0' = \frac{(1+e)\,p_0'}{\lambda-\kappa}d\varepsilon_v^p \tag{6}$$

3 | HYDRATE-CASM FORMULATION

The Hydrate-CASM extends the formulation of the CASM model[46] by implementing the subloading surface model[47] and introducing the densification mechanism. We note that material parameters e, v, p_0' and κ presented in Equations 1 to 5 read as e_{ah}, v_h, p_{0_h}' and κ_h in the presence of hydrate within the sediment.

3.1 | Hydrate-CASM subloading function

It is widely recognized that plastic strains can develop for stress states inside the yield surface; its interior is not a purely elastic domain. This feature results in a smooth transition between the elastic and the plastic response of soils.[58,59] González[60] shows that the CASM yield function reproduces well the residual soil strength but generally overestimates the elastic strains and predicts unrealistic sharp transitions between the elastic and elastoplastic states. The subloading surface concept[47] is implemented in the present formulation to account for pre-yield plasticity that allows capturing a smoother transition between elastic and plastic behavior, and a more accurate volumetric response of MHBS. This model assumes the existence of a subloading surface that expands/contracts inside the general yield surface keeping its same shape. The Hydrate-CASM subloading function is derived from Equation 2 as:

$$f = \left(\frac{q}{Mp'}\right)^n + \frac{1}{\ln(r)} ln\left(\frac{p'}{Rp'_{0_h}}\right) \tag{7}$$

where R controls the size of the subloading surface (Table 2) and recovers the original CASM yield function for values equal to 1. The evolution of R is controlled by the norm of the incremental plastic strain vector and the subloading parameter (u):

$$dR = -ulnR|d\boldsymbol{\varepsilon}^p| \tag{8}$$

3.1.1 | Plastic strain

The constitutive equation that characterizes an elasto-plastic material can be expressed as the following stress-strain relationship:

$$d\boldsymbol{\sigma}' = \boldsymbol{D}^e d\boldsymbol{\varepsilon}^e = \boldsymbol{D}^e (d\boldsymbol{\varepsilon} - d\boldsymbol{\varepsilon}^p) \tag{9a}$$

With:

$$\boldsymbol{D}^e = \begin{bmatrix} K+\frac{4}{3}G & K-\frac{2}{3}G & K-\frac{2}{3}G & 0 & 0 & 0 \\ K-\frac{2}{3}G & K+\frac{4}{3}G & K-\frac{2}{3}G & 0 & 0 & 0 \\ K-\frac{2}{3}G & K-\frac{2}{3}G & K+\frac{4}{3}G & 0 & 0 & 0 \\ 0 & 0 & 0 & G & 0 & 0 \\ 0 & 0 & 0 & 0 & G & 0 \\ 0 & 0 & 0 & 0 & 0 & G \end{bmatrix} \tag{9b}$$

$$d\boldsymbol{\varepsilon}^p = d\lambda^p \frac{\partial g}{\partial \boldsymbol{\sigma}'} \tag{9c}$$

The elastoplastic regime is reached when the stress state lies on the Hydrate-CASM yield surface. For the stress state to remain on it at any plastic loading, the consistency condition must be satisfied:

$$df(\boldsymbol{\sigma}'\boldsymbol{\chi}) = 0 \tag{10}$$

By linearizing the consistency condition, df can be rewritten as:

$$df = \left(\frac{\partial f}{\partial \boldsymbol{\sigma}'}\right)^T d\boldsymbol{\sigma}' + \left(\frac{\partial f}{\partial \boldsymbol{\chi}}\right)^T d\boldsymbol{\chi} = 0 \tag{11a}$$

with:

$$\frac{\partial f}{\partial \boldsymbol{\sigma}'} = \frac{\partial f}{\partial p'}\frac{\partial p'}{\partial \boldsymbol{\sigma}'} + \frac{\partial f}{\partial q}\frac{\partial q}{\partial \boldsymbol{\sigma}'} \tag{11b}$$

$$\frac{\partial f}{\partial \chi} = \left(\frac{\partial f}{\partial p'_{0_h}} + \frac{\partial f}{\partial R} \right) \quad (11c)$$

By solving Equations 9c and 10, the plastic multiplier is classically obtained as:

$$d\lambda^p = \frac{\left(\frac{\partial f}{\partial \boldsymbol{\sigma'}} \right)^T \boldsymbol{D}^e d\boldsymbol{\varepsilon}}{H + \left(\frac{\partial f}{\partial \boldsymbol{\sigma'}} \right)^T \boldsymbol{D}^e \frac{\partial \mathrm{g}}{\partial \boldsymbol{\sigma'}}} \quad (12a)$$

where:

$$H = -\left(\frac{\partial f}{\partial p'_{0_h}} \frac{\partial p'_{0_h}}{\partial d\boldsymbol{\varepsilon}^p_v} + \frac{\partial f}{\partial R} \frac{\partial R}{\partial |d\boldsymbol{\varepsilon}^p|} \right) \delta^T \frac{\partial \mathrm{g}}{\partial \boldsymbol{\sigma'}} \quad (12b)$$

$$\delta^T = \{1, 1, 1, 0, 0, 0\} \quad (12c)$$

3.2 | Densification mechanism

In nature, variations in the sediment void volume may result from two competing and interdependent processes: (a) mineral precipitation or dissolution (which compares here to hydrate formation and dissociation, respectively) and (ii) mechanical compaction or dilation under pressure.[61] In particular, mineral precipitation in pores reduces the sediment available void volume without experiencing mechanical compaction[62,63] and has a significant effect on its hydraulic and mechanical properties.[61,64]

Figure 3 examines qualitatively the effect of sediment density or void ratio on the magnitude of ξ and the corresponding mechanical behavior of the sediment under triaxial shear. For a reference sediment with positive ξ (grey cross in Figures 3A and 3B), an increase in density or a reduction of the void ratio reduces the vertical distance between the current state and the CSL (black cross in Figure 3B). Thus, during shear, the model predicts less hardening and contractancy than that observed on the reference sediment (Figure 3C). For a reference sediment with negative ξ (grey cross in Figures 3D and 3E), an increase in density increases the distance of the current state from the CSL (black cross in Figure 3E), and consequently, during shear, the model predicts a higher peak strength and greater dilatancy than that observed on the reference sediment (Figure 3F).

Figure 3 shows that variations in ξ related to an increase in sediment density produce a similar mechanical response than those observed in sediments with increasing hydrate saturation (ie, greater strength and dilatancy, or less contractancy, compared with the sediment without hydrate). Thus, we suggest that the occurrence of hydrate as a solid phase invading the voids of the hosting sediment may have a similar mechanical effect than the increase of the host sediment density. Alike Gupta et al,[65] the Hydrate-CASM formulation conceptually divides the sediment void-space into potential void volume (V_v) and available void volume (V_a) (Figure 4). The potential void volume is the space between the mineral grains of the sediment and includes the available void volume for fluid flow and storage and the hydrate volume.

To introduce the densification effect that pore invasion with hydrate has on the mechanical response of the sediment, the Hydrate-CASM uses the available void ratio left after hydrate formation (Equation 13) to derive the mechanical properties of the sediment.

$$e_{a_h} = e(1 - S_h) = e - e_h \quad (13)$$

From where, variations in ξ with hydrate saturation can be derived as:

$$d\xi = de_h \quad (14)$$

In addition to the reduction of sediment available void ratio, the presence of hydrate also enhances the sediment stiffness.[16,22,23] We represent the stiffening effect of hydrate on the elastic response of the sediment by the following explicit dependency between κ and S_h:
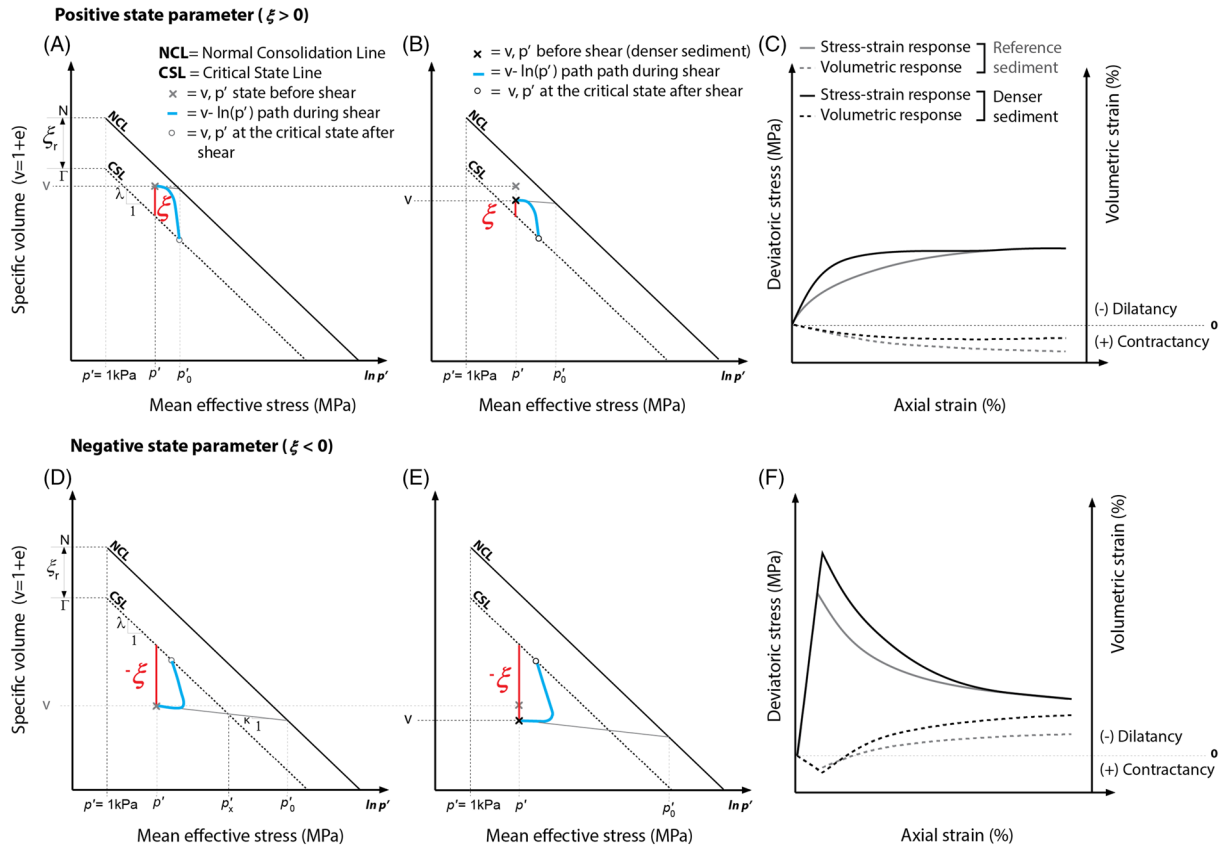
FIGURE 3 Effect of the increase in the sediment density on the magnitude of ξ and the corresponding stress-strain behavior of the sediment under triaxial shear. (A and D) Initial ξ for the reference sediments considered, (B and E) evolution of ξ due to densification, and (C and F) computed stress-strain sediment response at different densities
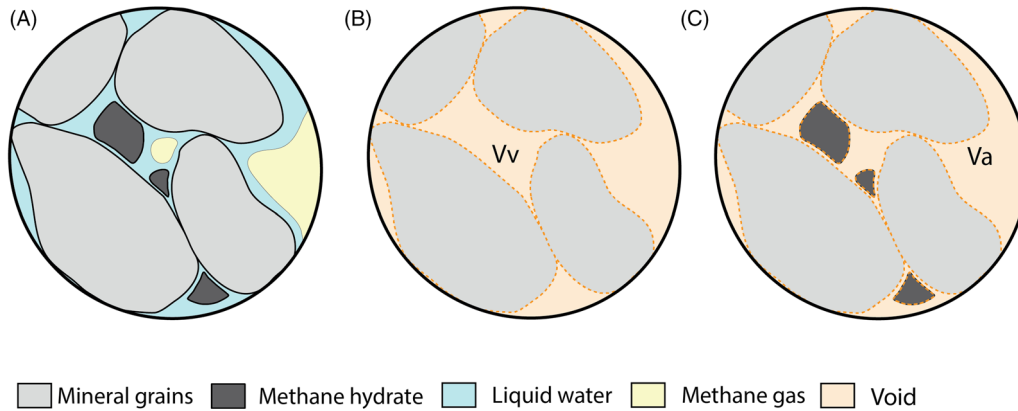

FIGURE 4 (A) Pore-scale phase distribution in methane hydrate-bearing sediment (MHBS), (B) potential void volume, and (C) available void volume. Note that $V_v = V_a$ for $S_h = 0$

$$\kappa_h = \kappa \, \kappa_{rf} \tag{15}$$

With:

$$\kappa_{rf} = \begin{cases} 1, S_h = 0 \\ 3S_h{}^2 - 2.68S_h + 0.9934, \ 0 < S_h \le 0.42 \\ 0.397, S_h > 0.42 \end{cases} \tag{16}$$

Equation 16 is obtained empirically by calibrating the experimental data of three synthetic sediments with hydrate saturations ranging from 24.2 to 53.1% (data examined in Section 4.2). This empirical relation needs validation for other sediments and hydrate saturations outside the range used for its determination.

The decrease of κ in MHBS has been recently observed in experimental high-pressure oedometer tests.[66] In our formulation, the use of κ_{rf} compensates for spurious changes of K (Equation 3a) when reducing the sediment available void ratio with increasing S_h. If neglecting the hydrate-related stiffening effect suggested in Equation 15, the Hydrate-CASM is still capable of reproducing a close solution to the experimental results (purple line in Figure 5B). However, the use of κ_h adopted in this work leads to a better fit of the elastic response and the peak strength of synthetic hydrate-bearing sediments subjected to triaxial shear (red line in Figure 5B).

As a result of both the decrease of the host sediment available void ratio and the increase of its stiffness during hydrate formation, a greater isotropic yield stress can be deduced graphically in the $v - \ln(p')$ space by projecting e_{ah} on the normal consolidation line (NCL) of the host sediment following the κ_h slope (Figure 5A), so that:

$$p'_{0_h} = exp\left(\frac{e_h}{\lambda - \kappa_h}\right) p'_0{}^{\left(\frac{\lambda - \kappa}{\lambda - \kappa_h}\right)} \tag{17a}$$

where changes in p'_{0_h} are computed through dp'_0, which reads:

$$dp'_0 = \frac{(1 + e_{ah})p'_0}{\lambda - \kappa} d\varepsilon_v^p \tag{17b}$$

3.2.1 | MHBS critical state

To evaluate the influence of the densification mechanism due to hydrate formation in the critical state of the sediment, Figure 6B relates the potential void ratio of the host sediment (e) with the isotropic yield stress predicted after hydrate formation (p'_{0h}).
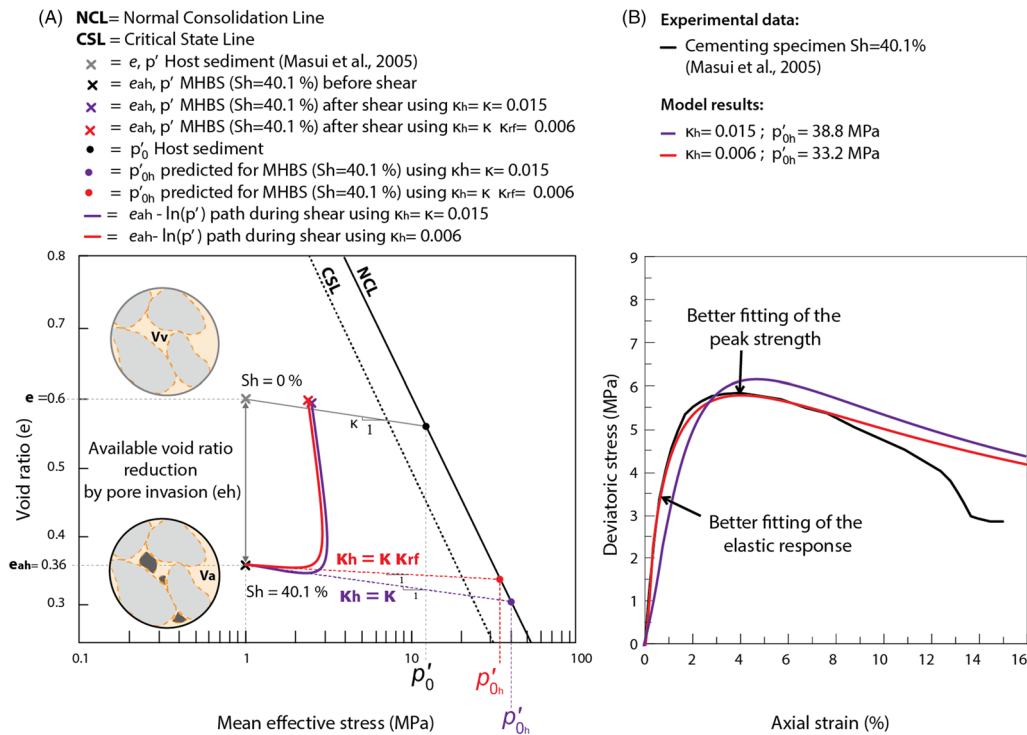

FIGURE 5 Influence of the densification and stiffening effects caused by hydrate formation in pores at (A) predicting the isotropic yield stress of methane hydrate-bearing sediment (MHBS) and at (B) capturing its mechanical response under triaxial shear (experimental data from Masui et al[19]). Note that the e_{ah}-$ln (p')$ paths are plotted here in terms of available void ratio
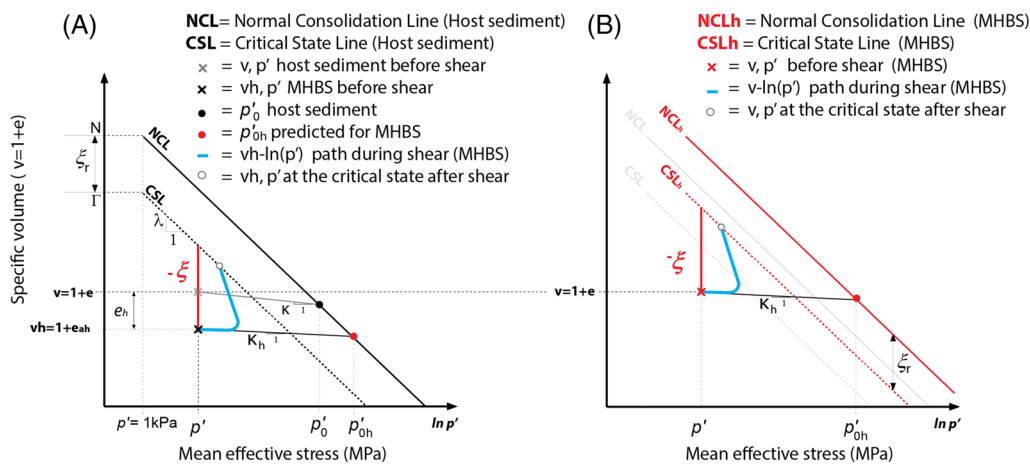
FIGURE 6 Effect of the densification mechanism at predicting (a) p′$_{0h}$ and (b) shifting both normal consolidation line (NCL) and critical state line (CSL) of the sediment

Figure 6A shows the procedure to obtain the isotropic yield stress of the MHBS (p'_{0h}), for which the sediment with hydrate is considered mechanically denser ($e_{ah} < e$) and stiffer ($\kappa_h < \kappa$) than the corresponding host sediment. When relating p'_{0h} with the potential void ratio of the sediment (e), both the NCL and CSL move to the right in the $v - \ln(p')$ space (Figure 6B). Thus, for a given S_h, the model predicts a normal consolidation line NCL$_h$ that is parallel to that for the host sediment (NCL) and that keeps a vertical distance from the CSL$_h$ equal to ξ_r (Table 2).

3.2.2 | Hydrate dissociation phenomena

Several experimental studies[67-72] and field observations[7-9,13,14] have demonstrated the impact of hydrate dissociation in the mechanical properties of MHBS. Hydrate dissociation occurs when the P-T and salinity conditions of the system are outside the hydrate stability zone. In the case of hydrate dissociation, the available void ratio of the sediment increases proportionally to the volume of hydrate dissociated, which in turn increases the sediment permeability and reduces its stiffness and strength.[22,73] Consequently, stress changes and mechanical deformation might be expected during specific conditions of hydrate dissociation. This aspect is integrated in the model since Equations 13 to 17b predict an increase in both e_{a_h} and κ_h, as well as a decrease in p'_{0_h} with decreasing S_h.

Figures 7 and 8 examine qualitatively the performance of the model in two different scenarios of thermal-induced hydrate dissociation under constant effective stress.

Figure 7 shows the ability of the model at predicting sediment collapse induced by hydrate dissociation after isotropic consolidation. Upon hydrate dissociation, the sediment is assumed to recover the mechanical properties of the host sediment (ie, NCL and CSL). Then, and as observed by Yoneda's et al.[66] observations, if after the hydrate dissociation the $v - \ln(p')$ state of the sediment is located in a mechanically inadmissible stress state (point 4 in Figure 7C), the model can predict sediment collapse until reaching a normally consolidated state (point 5 in Figure 7C).

Figure 8 examines the deformation properties of a hydrate-free specimen and a dissociated MHBS during triaxial shear. Initially, both sediments are isotropically consolidated up to p'_{iso} (Figures 8A and 8C). After consolidation, the MHBS is subjected to dissociation under constant effective stress (point 3, Figure 8D), so that the mechanical properties of the host sediment are recovered (ie, NCL and CSL, Figure 8D). Then, both sediments are sheared under drained conditions. In agreement with experimental observations in synthetic MHBS subjected to dissociation after isotropic consolidation,[73] our model predicts a lower failure strength for the MHBS after dissociation than that observed in the host sediment during shear (Figure 8E).

4 | HYDRATE-CASM PERFORMANCE

Triaxial tests at constant hydrate saturation provide very useful information to understand the influence of hydrate saturation on the mechanical behavior of MHBS. Two sets of stress-strain data from published triaxial tests are used
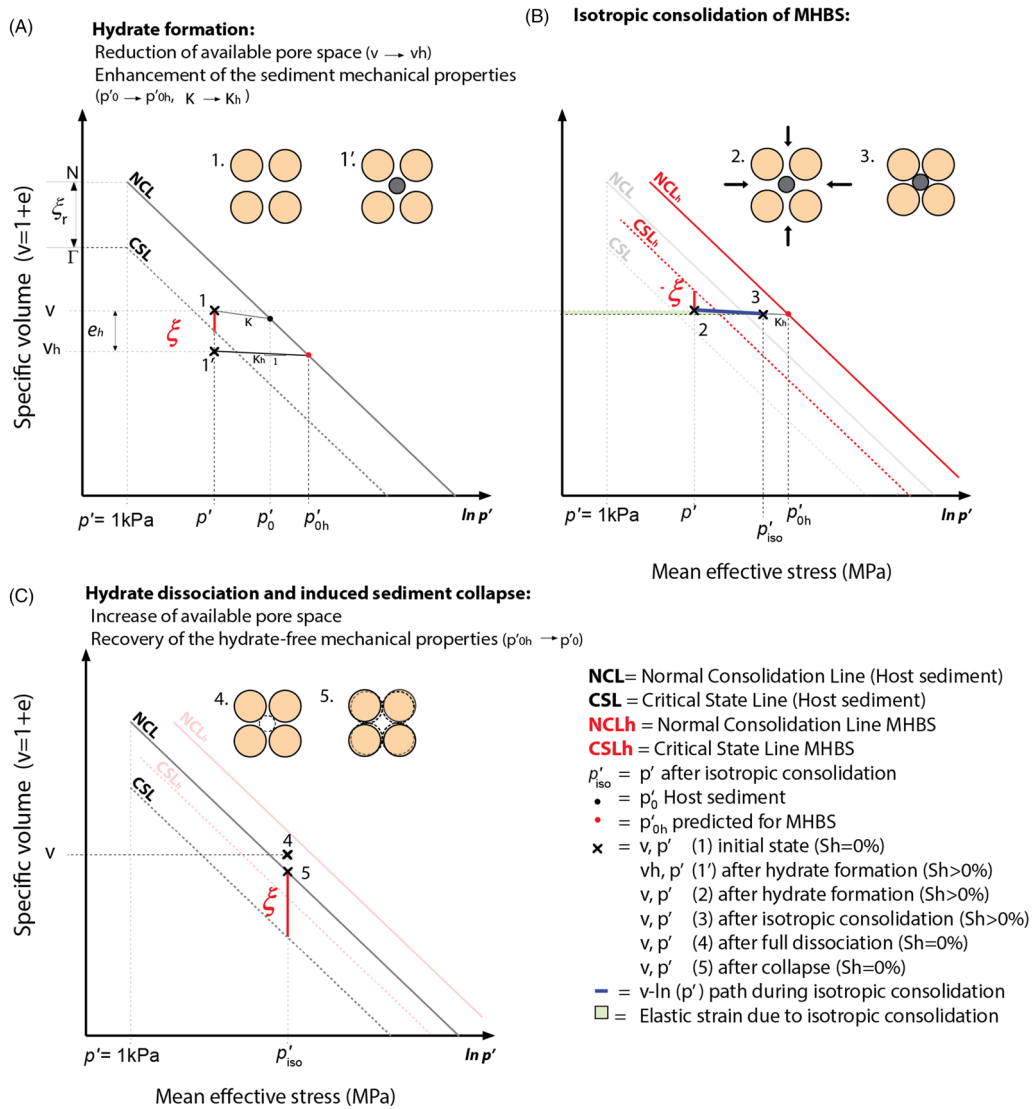
FIGURE 7 Qualitative analysis of sediment collapse due to hydrate dissociation after isotropic consolidation. A, Evolution of the host sediment available void ratio and increase of the isotropic yield stress due to hydrate densification effect. B, Prediction of the NCL_h and CSL_h characterizing the methane hydrate-bearing sediment (MHBS) and v-ln (p') evolution during isotropic consolidation. C, Sediment collapse induced by hydrate dissociation under constant effective stress. Pore-scale diagrams schematically depict the effect of hydrate formation, mechanical loading, hydrate dissociation, and collapse on the porous structure

here to evaluate the model performance. The selected experimental data report the mechanical behavior of synthetic MHBS subjected to drained triaxial shear at different confining effective stress, hydrate morphology, and saturation. These data have been widely used to calibrate previous mechanical models developed for MHBS, which allows us to compare the model results and validate our formulation.

4.1 | Modeling of Masui's et al (2005) experimental tests

Masui et al[19] conducted several triaxial tests on synthetic MHBS with different hydrate saturation and morphologies. Toyoura sand specimens with slightly different void ratios (Table 3) were used as host sediments for the synthetic formation of hydrate with cementing and pore-filling morphologies. Prior to forming hydrate, the host sediments were isotropically consolidated up to 1 MPa of confining effective stress. Then, the ice-seed method and the partial water saturation method were employed to produce hydrates with dominant pore-filling and cementing morphologies,
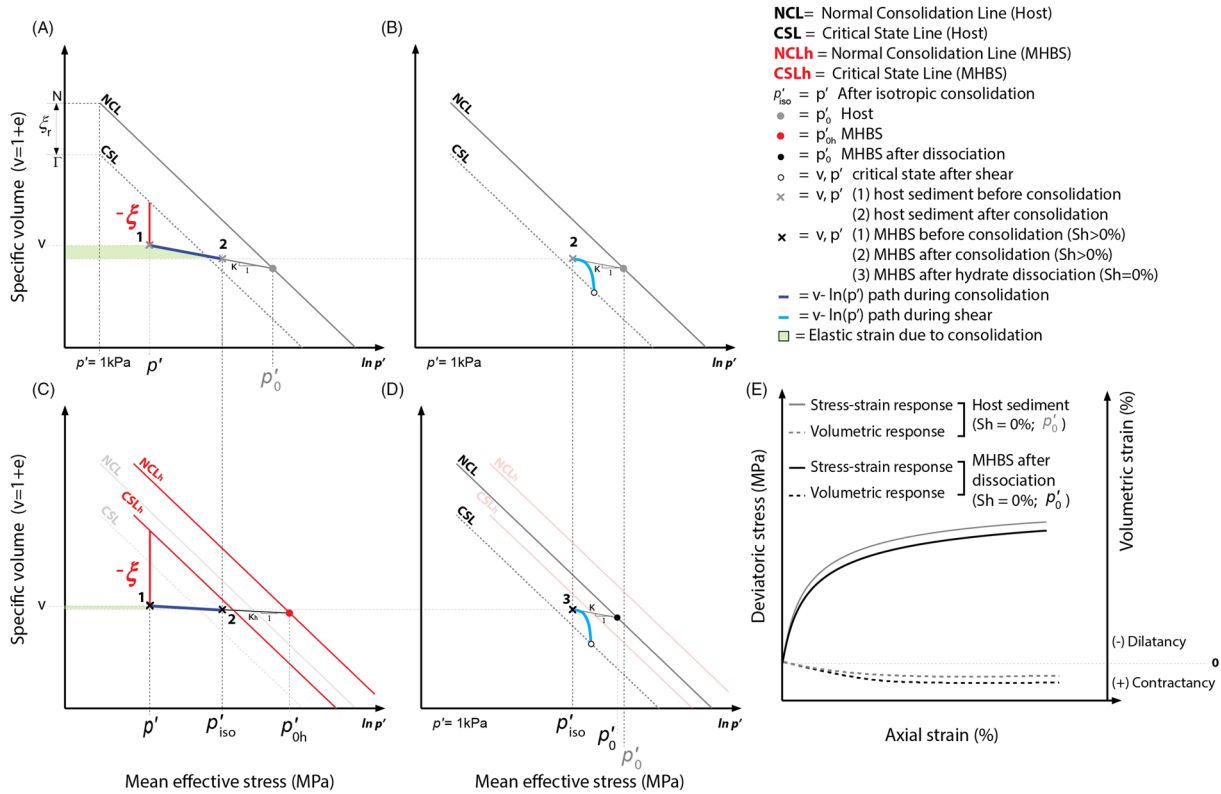
FIGURE 8 Qualitative analysis of changes in the stress-strain response of both host and dissociated methane hydrate-bearing sediment (MHBS) subjected to shear after isotropic consolidation. Evolution of the v-$ln(p')$ state during (A and C) isotropic consolidation, (B) triaxial shear of the host sediment, and (D) hydrate dissociation followed by triaxial shear of the dissociated MHBS. E, Computed mechanical response during triaxial shear

TABLE 3 Physical properties of Toyoura sand specimens used in Masui et al[19] as host sediment for the synthesis of cementing and pore-filling hydrates

	Host Sediment Physical Properties	
	Cementing Specimens	**Pore-Filling Specimens**
Diameter/height (mm)	50/100	50/100
Density (g/cm^3)	1.74-1.92	1.77-1.78
Void ratio	0.57-0.63	0.73-0.75

TABLE 4 Host sediment input parameters for modeling Masui et al[19] triaxial tests

Host Sediment Input Parameters									
e	λ	M	p'_0(MPa)	κ	υ	n	r	p'_{0_s}(MPa)	u
Cementing Specimens									
0.6	0.22	1.17	12	0.015	0.1	2.5	1.7	3.5	20
Pore-Filling Specimens									
0.75	0.22	1.17	5.3	0.015	0.1	2.5	1.7	3	20

respectively. After hydrate formation, the hydrate-bearing sand specimens were sheared at a constant rate of 0.1 % min^{-1} in drained conditions.

The set of critical state parameters characterizing the behavior of pure Toyoura sand (ie, hydrate-free sediment) (Table 4) has been calibrated here using the stress-strain curve and the volumetric response of the host specimen used
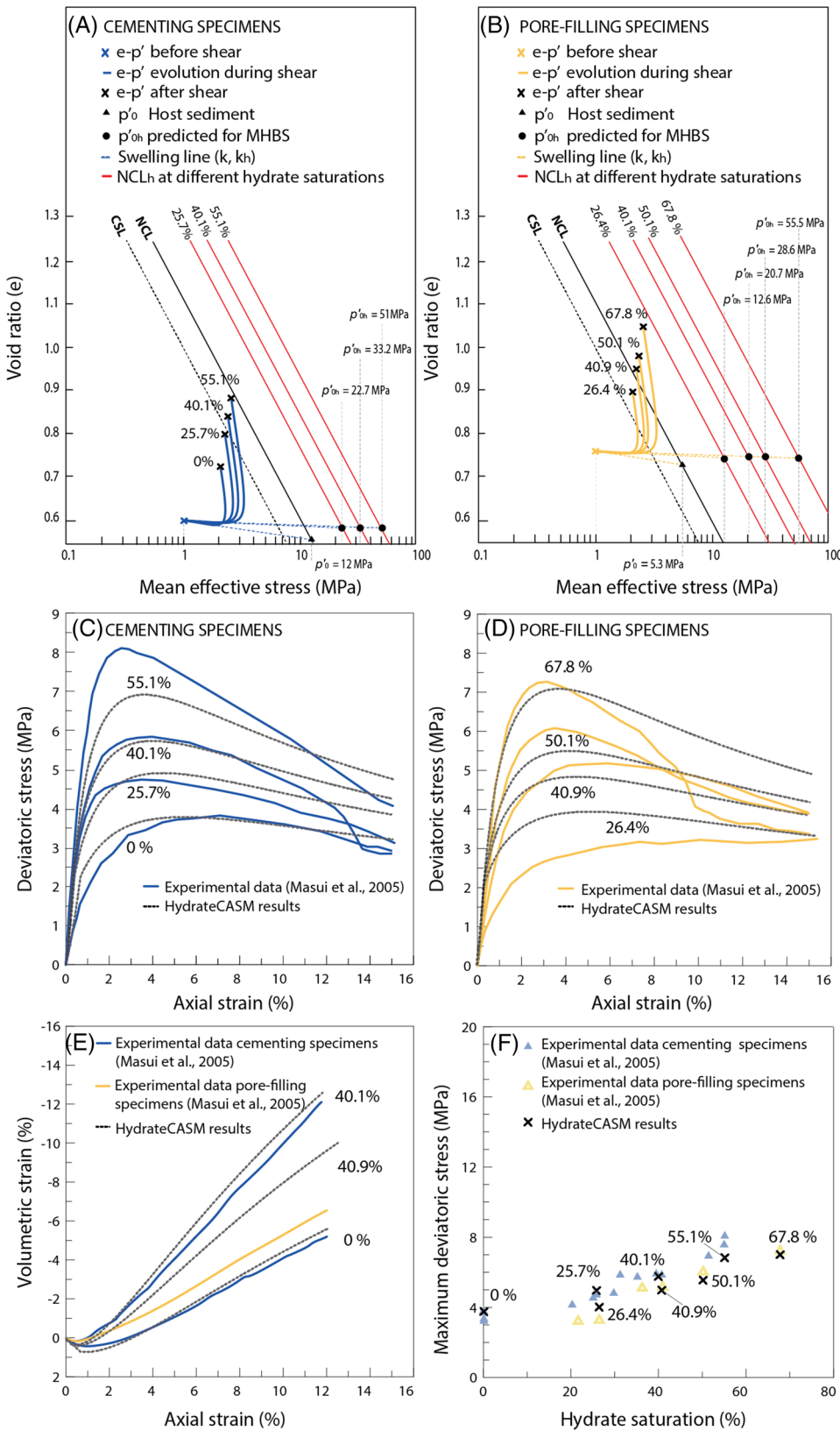
FIGURE 9 A and B, Effect of the host sediment void ratio and the hydrate saturation at shifting the normal consolidation line (NCL) of the sediment. Stress-strain behavior predicted during triaxial shear for (C) cementing and (D) pore-filling specimens. E, Volumetric response under triaxial shear of cementing specimens with $S_h = 0\%$ and 40.1% and pore-filling specimens with $S_h = 40.9\%$. F, Comparison of the sediment peak strength at different hydrate saturations predicted by the model and the corresponding experimental measurement. Percentages indicated in the figure correspond to hydrate saturations

for the synthetic formation of cementing hydrate ($S_h = 0\%$ in Figure 9C). For the calibration process, values adopted in previous publications that also model the mechanical response of Toyoura sand have been used as a reference.[35,39,79] In addition, the different void ratios of 0.6 and 0.75 reported for the cementing and pore-filling specimens, respectively, have also been considered in the simulations (Table 4).
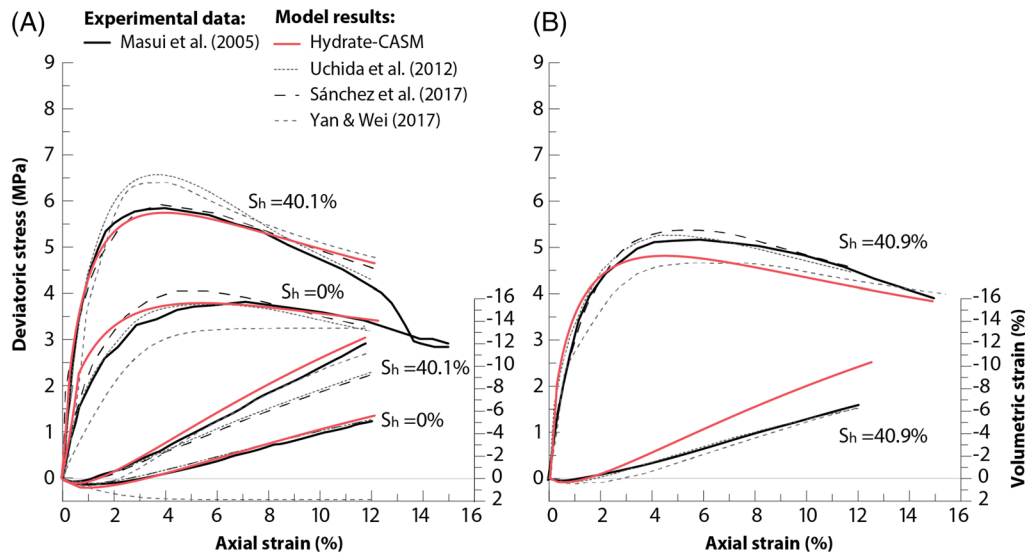
FIGURE 10 Model comparison between Hydrate-CASM predictions and those obtained from Uchida et al,[33] Sánchez et al,[35] and Yan and Wei[74] models against the experimental data from Masui et al[19] The results are presented in terms of stress-strain relationship and volumetric behavior for (A) cementing and (B) pore-filling specimens

TABLE 5 Host sediment input parameters for modeling Hyodo's et al[21] triaxial tests at 1, 3, and 5 MPa of confining effective stress

Host Sediment Input Parameters									
e	λ	M	p'_0 (MPa)	κ	υ	n	r	p'_{0_s} (MPa)	u
0.65	0.22	1.32	9	0.015	0.1	4	2.5	5.6	50

Figure 9 shows the model results for Masui's et al[19] triaxial tests. Overall, our results are satisfactory if one keeps in mind the simplicity of the model formulation in terms of the number of input parameters required. The Hydrate-CASM successfully captures the trend and magnitude of the mechanical response of MHBS subjected to shear, showing an increase in stiffness, shear strength, and dilatancy with increasing S_h (Figures 9C-9F). The model outputs fit particularly well the volumetric response of the cementing specimens (Figure 9E) as well as the rate of increase observed in the peak strength with S_h (Figure 9F). However, they underestimate the maximum deviatoric stress of the cementing specimen with $S_h = 55.1\%$ (Figure 9C) and slightly overestimate the maximum deviatoric stress of the pore-filling specimen with $S_h = 26.4\%$ (Figure 9D) and the volumetric response of the pore-filling sediment with $S_h = 40.9\%$ (Figure 9E).

Previous mechanical models for MHBS that also modeled Masui's et al[19] experimental data[33,35,74] assume that the differences in strength and dilatancy observed between cementing and pore-filling specimens for a given hydrate saturation are controlled by hydrate morphology. However, Masui et al[19] state that if the pore hydrate saturation is the same in both types of specimens (eg, $S_h \approx 40\%$ in Figures 9C and 9D), shear strength becomes higher for the specimen with lower void ratio. The similarity between the results from previous models and those obtained with the Hydrate-CASM (Figure 10), which does not consider mechanical contributions related to hydrate morphology, suggests that the different mechanical behavior between cementing and pore-filling specimens can be alternatively reproduced considering the different void ratios reported for each set of the host specimens (Table 3).

4.2 | Modeling of Hyodo's et al (2013) experimental tests

Hyodo et al[21] performed a series of triaxial tests to investigate the mechanical properties and dissociation characteristics of synthetic MHBS. They used an innovative temperature controlled high-pressure apparatus specially developed to reproduce the in situ conditions expected during gas extraction from hydrates. Three sets of triaxial tests conducted at zero or constant hydrate saturation are used here for the model application. The tests were performed on Toyoura sand
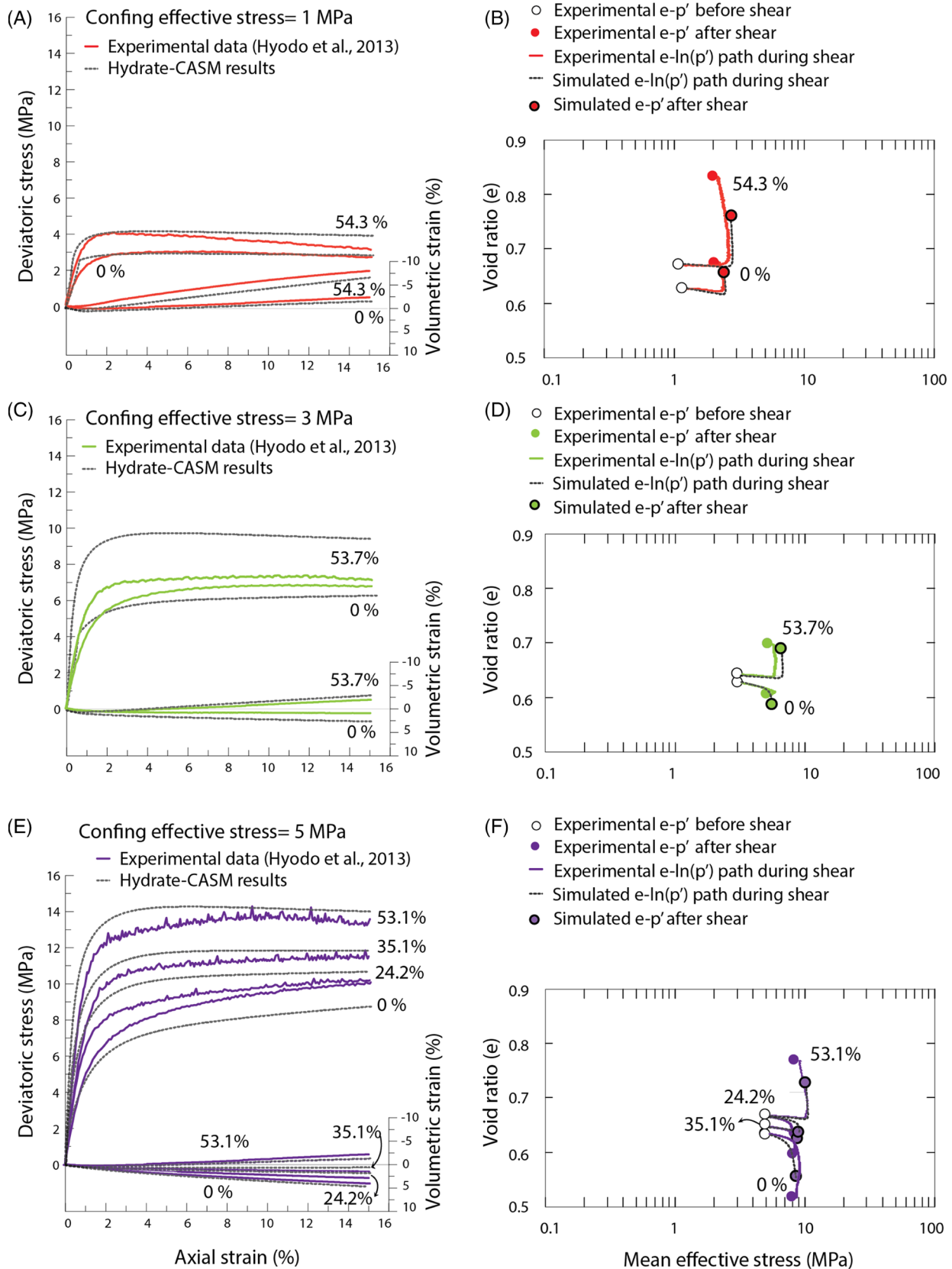
FIGURE 11 Modeling of Hyodo's et al[21] experimental data. Results are presented in terms of deviatoric stress-axial strain, volumetric strain-axial strain, and void ratio-mean effective stress relationships at effective confining stress of (A and B) 1 MPa, (C and D) 3 MPa, and (E and F) 5 MPa. For comparison purposes, the *e-ln(p')* paths during triaxial shear are adjusted to the potential void ratio reported by Hyodo et al[21] after isotropic consolidation. Percentages indicated in the figure correspond to hydrate saturations
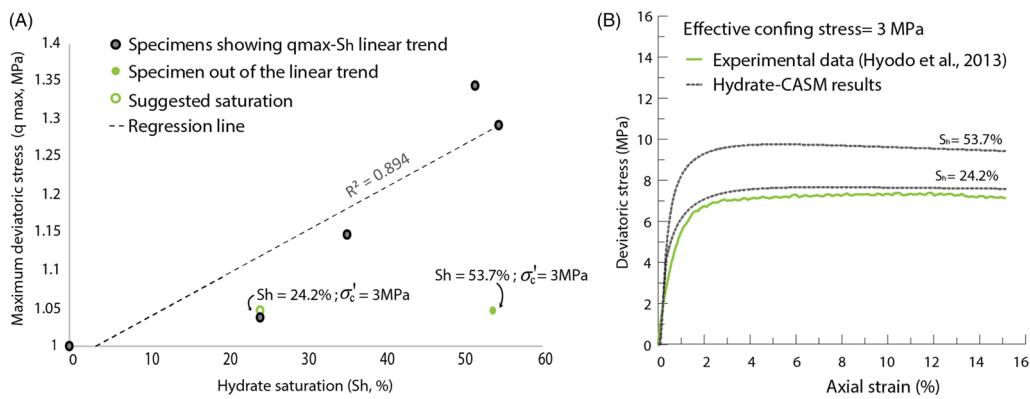
FIGURE 12 Effect of hydrate saturation on the peak strength of methane hydrate-bearing sediment (MHBS). A, q_{max}-S_h relatively linear trend for Hyodo's et al[21] experimental data. Note that the maximum deviatoric stress is normalized by the value reported in the corresponding sediment without hydrate. B, Model predictions considering both S_h=53.7% and S_h=24.2% for the sediment confined at 3MPa
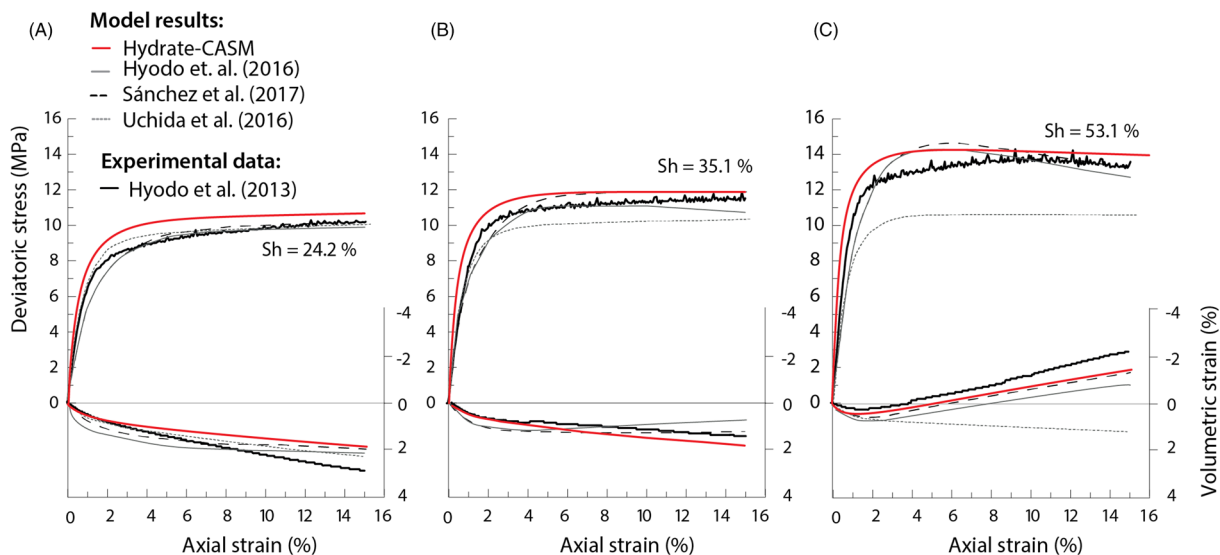

FIGURE 13 Model comparison between the results from Hydrate-CASM, Sánchez et al,[35] Hyodo et al,[48] and Uchida et al[79] models against the experimental data from Hyodo et al.[21] Stress-strain behavior and volumetric response for hydrate-bearing sediments with (A) S_h=24.2%, (B) S_h=35.1%, and (C) S_h=53.1% subjected to triaxial shear under confining effective stress of 5 MPa

with an initial porosity of about 40% ($e \approx 0.65$), subjected to confining effective stress of 1, 3, and 5 MPa with different hydrate saturations. The experimental data from the host sediments (ie, hydrate-free specimens) are used to calibrate the critical state parameters of the model (Table 5) and those from the hydrate-bearing sand are used to examine the model capability at capturing the mechanical effect of S_h.

Figure 11 shows the simulation of the experimental tests performed by Hyodo et al.[21] The results show the capability of the Hydrate-CASM at capturing changes in the mechanical response of the host sediment with increasing confining effective stress. For the host sediment confined at 1 MPa, the model predicts a moderate softening after a peak and the volumetric strain goes from compressive to slightly dilatant ($S_h = 0\%$; Figure 11A). With increasing effective stress, the model predicts a gradual transition of this response towards a hardening and a fully contracting behavior, although the maximum deviatoric stress at 3 and 5 MPa are slightly underestimated ($S_h = 0\%$; Figures 11C and 11E). The results for the hydrate-bearing sand show, in general, a good agreement with the experimental data, capturing both the trend and magnitude of the stress-strain and volumetric responses of the sediment (Figures 11A, 11C, and 11E) and the $e - \ln(p')$ paths during triaxial shear (Figures 11B, 11D, and 11F). However, the model largely overestimates the peak strength for the sediment with $S_h = 53.7\%$ tested at 3 MPa (Figure 11C).

The maximum strength of the sediments examined in this section tends to increase almost linearly with hydrate saturation. However, the sediment with $S_h = 53.7\%$ does not follow this trend (Figure 12A). Hyodo et al[21] estimated the hydrate saturation within the sediment based on the stoichiometry of the hydrate formation reaction and assuming that all the methane gas injected converted into hydrate. Several studies have proposed that hydrate and gas can coexist under hydrate stability conditions.[75-77] In particular, Sahoo et al[78] show experimental evidence in which hydrate formation stops with up to 13% of gas still on the sediment under favorable pressure, temperature, and salinity conditions. Accordingly, we hypothesize that it is possible that part of the gas injected into the specimen with $S_h=53.7\%$ could not form hydrate, and consequently, the saturation reported could have been slightly overestimated. For comparison purposes, the same test was modeled considering $S_h= 24.2\%$, which is a more consistent value within the linear $q_{max} - S_h$ trend observed for the rest of the experimental data (Figure 12A). Considering $S_h= 24.2\%$, the Hydrate-CASM reproduces closely the deviatoric stress-axial strain relationship reported experimentally (Figure 12B).

The results presented in this section have been validated against the outputs from three other mechanical models for MHBS[35,48,79] (Figure 13). The comparison is satisfactory and shows that despite the simplicity of the densification mechanism, the Hydrate-CASM performs similarly to models that require more than one hydrate-related empirical parameter in their formulation.

5 | CONCLUSIONS

The Hydrate-CASM is a new elastoplastic constitutive model developed to simulate the mechanical behavior of MHBS. This model extends the formulation of the CASM model by implementing the subloading surface model and introducing the densification mechanism. Alternatively to bonding or cementing models, the Hydrate-CASM suggests that the greater strength and dilatancy observed in MHBS can be explained by the densification and stiffening effects that pore invasion with hydrate has on the mechanical properties of the sediment. The densification mechanism attributes hydrate-related changes in the host sediment available void ratio, swelling line slope, and isotropic yield stress to sediment stress-strain changes. Moreover, the flexibility in the shape of the Hydrate-CASM yield function and the use of a nonassociated flow rule make our formulation particularly suitable for modeling the behavior of sands, the most likely target deposit for commercial exploitation of hydrates.

Compared with previous models for MHBS, our formulation reduces to one the number of empirical hydrate-dependent parameters required to reasonably capture the mechanical behavior of MHBS. The Hydrate-CASM only requires an empirical hydrate-dependent parameter to express changes in the sediment swelling line slope with hydrate saturation. Reducing to one the number of these parameters is an important advance in mechanical constitutive modeling of MHBS (a) because obtaining them through laboratory tests is challenging, especially if their physical meaning is not well understood, and (b) because eases the application of the Hydrate-CASM model to a wide range of experimental test conditions.

Robust and well-described published experimental tests have been chosen to calibrate the Hydrate-CASM capabilities at modeling the mechanical behavior of MHBS during triaxial shear. These tests cover the most relevant conditions related to MHBS behavior, including a wide range of hydrate saturations, several hydrate morphologies, and confinement stress. In addition, they have been previously used to calibrate other mechanical models developed for MHBS, which allowed us to compare and validate our results. Our simulations evidence the ability of the Hydrate-CASM to predict both stress-strain and the volumetric response of synthetic MHBS subjected to triaxial shear and suggest that quantifying the void ratio and the mechanical response of the host sediment is key to isolate hydrate-related mechanical contributions.

ORCID

Maria De La Fuente https://orcid.org/0000-0002-5688-1877
Jean Vaunat https://orcid.org/0000-0003-3579-9652
Héctor Marín-Moreno https://orcid.org/0000-0002-3412-1359

REFERENCES

1. Holder GD, Kamath VA, Godbole SP. The potential of natural gas hydrates as an energy resource. *Annual Review of Energy*. 1984;9: 427-445.

2. Grauls D. Gas hydrates: Importance and applications in petroleum exploration. *Mar Pet Geol*. 2001;18:519-523.

3. Collett TS. Energy resource potential of natural gas hydrates. *AAPG Bull*. 2002;86(11):1971-1992.

4. Dallimore SR, Collett TS. Summary and implications of the Mallik 2002 Gas Hydrate Production Research Well Program. In Scientific results from the Mallik 2002 Gas Hydrate Production Research Well Program, Mackenzie Delta, Northwest Territories, Canada. In: Dallimore SR, Collett TS, eds. *Bulletin 585*. Ottawa, Ontario: Geological Survey of Canada; 2005.

5. Ruppel C. Tapping methane hydrates for unconventional natural gas. *Elements*. 2007;3:193-199.

6. Nagel N. Compaction and subsidence issues within the petroleum industry: from Wilmington to Ekofisk and beyond. Physics and Chemistry of the Earth 2001; Part A. *Solid Earth and Geodesy*. 26(1-2):3-14. 7.

7. Freij-Ayoub R, Tan C, Clennell B, Tohidi B, Yang J. A wellbore stability model for hydrate bearing sediments. *J Petrol Sci Eng*. 2007; 57(1–2):209-220.

8. Yamamoto K, Dallimore S. Aurora-JOGMEC-NRCan Mallik 2006-2008 Gas Hydrate Research Project Progress. *Fire in Ice, Methane Hydrate Newsletter, National Energy Technology Laboratory*. 2008;8:1-20.

9. Dickens GR, O'Neil JR, Rea DK, Owen RM. Dissociation of oceanic methane hydrate as a cause of the carbon isotope excursion at the end of the Paleocene. *Paleoceanography*. 1995;19:965-971.

10. Archer D. Methane hydrate stability and anthropogenic climate change. *Biogeosciences*. 2007;4:521-544.

11. Ruppel C, Pohlman JW. *Climate change and the global carbon cycle: Perspectives and opportunities, Fire in the Ice: Methane Hydrate Newsletter 2008; winter, pp. 5 – 8, Off. of Fossil Energy, Natl*. Washington, D. C: Energy Technol. Lab., U.S. Dep. of Energy.

12. Minshull TA, Marín-Moreno H, Armstrong McKay DI, Wilson PA. Mechanistic insights into a hydrate contribution to the Paleocene-Eocene carbon cycle perturbation from coupled thermohydraulic simulations. *Geophys Res Lett*. 2016;43(16):8637-8644.

13. Sultan N, Cochonat P, Foucher JP, Mienert J. Effect of gas hydrates melting on seafloor slope instability. *Mar Geol*. 2004;213:379-401.

14. Pecher I. a., Henrys, S. a., Ellis, S., Chiswell, S. M. and Kukowski, N. Erosion of the seafloor at the top of the gas hydrate stability zone on the Hikurangi Margin, New Zealand. *Geophys Res Lett*. 2005;32(24):3-6.

15. Paull CK, Ussler W, Dallimore SR, et al. Origin of pingo-like features on the Beaufort Sea shelf and their possible relationship to decomposing methane gas hydrates. *Geophys Res Lett*. 2007;34(1):1-5.

16. Priest JA. A laboratory investigation into the seismic velocities of methane gas hydrate-bearing sand. *J Geophys Res*. 2005;110(B4):1-13.

17. Winters W, Waite W, Mason D, Gilbert L, Pecher I. Methane gas hydrate effect on sediment acoustic and strength properties. *J Petrol Sci Eng*. 2007;56(1-3):127-135.

18. Priest JA, Rees EVL, Clayton CRI. Influence of gas hydrate morphology on the seismic velocities of sands. *J Geophys Res*. 2009;114(B11): 1-13.

19. Masui A, Haneda H, Ogata Y, Aoki K. The effect of saturation degree of methane hydrate on the shear strength of synthetic methane hydrate sediments, Proceedings of the 5th International Conference on Gas Hydrates, Trondheim, Norway 2005; vol. 2037, pp. 657–663.

20. Miyazaki K, Masui A, Sakamoto Y, Aoki K, Tenma N, Yamaguchi T. Triaxial compressive properties of artificial methane-hydrate-bearing sediment. *J Geophys Res Solid Earth*. 2011;116(6):1-11.

21. Hyodo M, Yoneda J, Yoshimoto N, Nakata Y. Mechanical and dissociation properties of methane hydrate-bearing sand in deep seabed. *Soils and Foundations*. 2013;53(2):299-314.

22. Soga K, Lee SL, Ng MYA, Klar A. *Characterisation and engineering properties of methane hydrate soils, Characterization and Engineering Properties of Natural Soils 2006; vol. 4, edited by K. Soga et al., pp*. London, U. K: Taylor and Francis:2591-2642.

23. Waite WF, Santamarina JC, Cortes DD, Dugan B, Espinoza DN. Germaine, et al. *Physical Properties of Hydrate-Bearing Sediments Rev Geophys*. 2009;47:1-38, RG4003.

24. Hannegan, D., Todd, R. J., Pritchard, D. M. & Jonasson, B. Uniquely applicable to methane hydrate drilling. In: SPE/IADC Underbalanced Technology Conference and Exhibition. Houston, USA 2004.

25. McIver RD. Role of naturally occurring gas hydrates in sediment transport. *The American Association of Petroleum Geologist Bulletin*. 1982;66(6):789-792.

26. Kayen, R.E., and Lee, H.J. Slope stability in regions of sea-floor gas hydrate; Beaufort Sea continental slope, in Schwab, W.C. 1993.

27. Nixon MF, Grozic JLH. Submarine slope failure due to gas hydrate dissociation: a preliminary quantification. *Can Geotech J*. 2007;44: 314-325.

28. Borowski, W. S. & Paul, C. K. The gas hydrate detection problem: recognition of shallow-subbottom gas hazards in deep-water areas. In: Off-shore Technology Conference. Houston, USA, 1997: Offshore Technology Conference.

29. Klar A, Soga K, Ng MY. a. Coupled deformation–flow analysis for methane hydrate extraction. *Géotechnique*. 2010;60(10):765-776.

30. Jung JW, Santamarina JC, Soga K. Stress-strain response of hydrate-bearing sands: numerical study using discrete element method simulations. *J Geophys Res Solid Earth*. 2012;117(4):1-12.

31. Pinkert S, Grozic JLH. Prediction of the mechanical response of hydrate-bearing sands. *J Geophys Res Solid Earth*. 2014;4695-4707.

32. Pinkert S, Grozic JLH, Priest JA. Strain-softening model for hydrate-bearing sands. *International Journal of Geomechanics*. 2015;15(6): 1-6.

33. Uchida S, Soga K, Yamamoto K. Critical state soil constitutive model for methane hydrate soil. *J Geophys Res Solid Earth*. 2012;117(B3): 1-13.

34. Sánchez M, Gai X. Geomechanical and numerical modeling of gas hydrate sediments. *Energy Geotechnics*. 2016;19-24.

35. Sánchez M, Gai X, Santamarina JC. A constitutive mechanical model for gas hydrate bearing sediments incorporating inelastic mechanisms. *Computers and Geotechnics*. 2017;84:28-46.

36. Sultan, N., and Garziglia, S. Geomechanical constitutive modelling of gas-hydrate bearing sediments. The 7th International Conference on Gas Hydrates, (ICGH) 2011.

37. De La Fuente M, Vaunat J, Marín-Moreno H. Composite model to reproduce the mechanical behaviour of methane hydrate bearing sediments. *Energy Geotechnics*. 2016;483-489.

38. Jiang M, Zhu F, Liu F, Utili S. A bond contact model for methane hydrate-bearing sediments with interparticle cementation. *International Journal for Numerical and Analytical Methods in Geomechanics 2014*. 2014;38(17):1823-1854.

39. Lin JS, Seol Y, Choi JH. An SMP critical state model for methane hydrate-bearing sands. *International Journal for Numerical and Analytical Methods in Geomechanics*. 2015;32(9):969-987.

40. Chaouachi M, Falenty A, Sell K, et al. Microstructural evolution of gas hydrates in sedimentary matrices observed with synchrotron x-ray computed tomographic microscopy. *GeochemGeophy Geosy*. 2015;16:1711-1722.

41. Sahoo SK, Madhusudhan BN, Marin-Moreno H, et al. Laboratory insights into the effect of sediment-hosted methane hydrate morphology on elastic wave velocity from time lapse 4D synchrotron X-ray computed tomography. *Geochem Geophys Geosyst*. 2018; 19(11):4502-4521.

42. Sell, K., Saenger, H., Quintal, B., and Enzmann, F., K. M. Digital lab of hydrate-bearing sediments: determination of effective elastic properties on the microscale. European Geosciences Union - General Assembly 2017

43. Pinkert S. Rowe's stress-dilatancy theory for hydrate-bearing sand. *International Journal of Geomechanics*. 2016;17(1):6016008.

44. Pinkert S. The lack of true cohesion in hydrate-bearing sands. *Granular Matter*. 2017;19(3):1-11. https://doi.org/10.1007/s10035-017-0742-5

45. Pinkert S, Grozic JLH. Experimental verification of a prediction model for hydrate bearing sand. *J Geophys Res Solid Earth*. 2016; 121(October):4147-4155.

46. Yu HS. CASM: a unified state parameter model for clay and sand. *International Journal for Numerical and Analytical Methods in Geomechanics*. 1998;22(8):621-653.

47. Hashiguchi K. Subloading surface model in unconventional plasticity. *Int J Solids Struct*. 1989;25(8):917-945.

48. Hyodo, M., Nakata, Y., and Yoshimoto, N. Challenge for methane hydrate production by geotechnical engineering. Proceeding of the 15th Asian Regional Conference on Soil Mechanics and Geotechnical Engineering 2016; 62–75.

49. Boswell R, Collett TS. Current perspectives on gas hydrate resources. *Energ Environ Sci*. 2011;4:1206-1215.

50. Been K, Jefferies MG. A state parameter for sands. *Géotechnique*. 1985;35(2):99-112.

51. Graham J, Crooks JHA, Bell A. L Time effects on the stress-strain behaviour of natural soft clays. *Geotechnique*. 1983;33(3):327-340.

52. Lade, B. P. V, and Nelson, R. B. Non-Associated flow and stability of granular materials. *J Eng Mech*,1988; 113(9), 1302–1318.

53. Roscoe KH, Schofield AN, Wroth CP. On the yielding of soils. *Geotechnique*. 1958;8(1):22-53.

54. Roscoe KH, Burland JB. In: Heyman J, Leckie FA, eds. *On the generalized stress-strain behaviour of wet clays, in Engineering Plasticity. Edited by*. Cambridge, England: Cambridge Univ. Press; 1968:535-609.

55. Nova R, Wood DM. An experimental program to define yield function for sand. *Soils and Foundations*. 1978;18(4):77-86.

56. Chandler HW. A plasticity theory without Drucker's postulate for granular materials. *J Mech Phys Solids*. 1985;33:215-226.

57. Rowe PW. The stress-dilatancy relation for static equilibrium of an assembly of particles in contact. *Proc Roy Soc*. 1962;267:500-527.

58. Jardine RJ. Some observations on the kinematic nature of soil stiffness. *Soils Found*. 1992;32(2):111-124.

59. Mitchell JK, Soga K. *Fundamentals of soil behaviour*. Hoboken, N.J: John Wiley; 2005.

60. González N. *Development of a family of constitutive models for geotechnical applications*. Barcelona (Spain), (May: PhD thesis, Polytechnic University of Catalonia; 2011.

61. Vialle S, Vanorio T. Laboratory measurements of elastic properties of carbonate rocks during injection of reactive CO_2-saturated water. *Geophys Res Lett*. 2011;38:1-5, L01302.

62. Nygaard, R., Bjørlykke, K., Høeg, K., Hareland, G. The effect of diagenesis on stress-strain behavior and acoustic velocities in sandstones. Proceedings of the 1st Canada-US Rock Mechanics Symposium-Rock Mechanics Meeting Society's Challenges and Demands 2007.

63. Pinyol Puigmartí NM, Vaunat J. Alonso Pérez de Agreda, E. A constitutive model for soft clayey rocks that includes weathering effects. *Geotechnique*. 2007;57(2):137-151.

64. Chagneau A, Claret F, Enzmann F, et al. Mineral precipitation-induced porosity reduction and its effect on transport parameters in diffusion-controlled porous media. *Geochemical Transactions, Chemistry Central*. 2015;16(1):16.

65. Gupta S, Helmig R, Wohlmuth B. Non-isothermal, multi-phase, multi-component flows through deformable methane hydrate reservoirs. *Comput Geosci*. 2015;19:1063-1088. https://doi.org/10.1007/s10596-015-9520-9

66. Yoneda, J., Oshima, M., Kida, M., Kato, A., Konno, Y., Jin, Y., Tenma, N. *Consolidation and hardening behavior of hydrate-bearing pressure-core sediments recovered from the Krishna–Godavari Basin, offshore India, Marine and Petroleum Geology*. 2018, ISSN 0264-8172.

67. Masui A, Haneda H, Ogata Y, Aoki K. *Mechanical properties of sandy sediment containing marine gas hydrates in deep sea offshore Japan survey drilling in Nankai Trough. In Proceedings of Seventh ISOPE Ocean Mining Symposium*. Lisbon, Portugal: International Society of Offshore and Polar Engineers; 2007:53-56.

68. Lu W, Chou IM, Burruss RC. Determination of methane concentrations in water in equilibrium with sI methane hydrate in the absence of a vapor phase by in situ Raman spectroscopy. *Geochim Cosmochim Acta*. 2008;72:412-422.

69. Lee JY, Santamarina JC, Ruppel C. *Volume change associated with formation and dissociation of hydrate in sediment*. Geophysics, Geosystems: Geochemistry; 2010 11(3).

70. Hyodo, M., Kajiyama S., Yoshimoto, N., Nakata, Y. Triaxial behaviour of methane hydrate bearing sand. Proceedings of 10th Int. ISOPE Ocean Mining & Gas Hydrate Symposium OMS-2013, Szczecin, Poland, 2014; 126-134.

71. Santamarina JC, Dai S, Terzariol M, et al. Hydro-bio-geomechanical properties of hydrate-bearing sediments from Nankai Trough. *Mar Pet Geol*. 2015;66:1-17.

72. Song YC, Zhu YM, Liu WG, Li YH, Lu Y, Shen ZT. The effects of methane hydrate dissociation at different temperatures on the stability of porous sediments. *J Petrol Sci Eng*. 2016;147(May):77-86.

73. Hyodo M, Li Y, Yoneda J, Nakata Y, Yoshimoto N, Nishimura A. Effects of dissociation on the shear strength and deformation behavior of methane hydrate-bearing sediments. *Marine and Petroleum Geology*. 2014;51:52-62. ISSN 0264-8172

74. Yan R, Wei C. Constitutive model for gas hydrate–bearing soils considering hydrate occurrence habits. *International Journal of Geomechanics*. 2017;17(8):4017032.

75. Milkov AV. Global estimates of hydrate-bound gas in marine sediments: how much is really out there? *Earth Sci Rev*. 2004;66:183-197.

76. Darnell KN, Flemings PB. Transient seafloor venting on continental slopes from warming-induced methane hydrate dissociation. *Geophys Res Lett*. 2015;42:10765-10772.

77. Goswami BK, Weitemeyer KA, Minshull TA, et al. A joint electromagnetic and seismic study of an active pockmark within the hydrate stability field at the Vestnesa Ridge, West Svalbard margin. *J Geophys Res Solid Earth*. 2015;120:6797-6822.

78. Sahoo S, Marín-Moreno H, North L, et al. Presence and consequences of coexisting methane gas with hydrate under two phase water-hydrate stability conditions. *J Geophys Res Solid Earth*. 2018:3377-3390. https://doi.org/10.1029/2018JB015598

79. Uchida S, Xie X-G, Leung YF. Role of critical state framework in understanding geomechanical behaviour of methane hydrate-bearing sediments. *J Geophys Res*. 2016;121(8):5580-5595.